Tectonophysics 882 (2024) 230360

Contents lists available at ScienceDirect

Tectonophysics

journal homepage: www.elsevier.com/locate/tecto

# Azimuthal seismic anisotropy in the crust beneath the Granada Basin (Spain)

I. Serrano [a,b,*], M.A. Dengra [a], F. Torcal [c], D. Zhao [d]

[a] Instituto Andaluz de Geofísica, Universidad de Granada, Spain
[b] Departamento de Física Teórica y del Cosmos, Facultad de Ciencias, Spain
[c] Departamento de Sistemas Físicos, Químicos y Naturales, Universidad Pablo de Olavide, Sevilla, Spain
[d] Department of Geophysics, Graduate School of Science, Tohoku University, Sendai, Japan

ARTICLE INFO

*Keywords:*
Seismic tomography
Seismic anisotropy
Earthquake
Fault
Atarfe-Santa Fe seismic series
Betic Cordillera

ABSTRACT

In this research, we conducted the first P-wave tomographic imaging of 3-D azimuthal anisotropy of the Granada Basin (Betic Cordillera, Spain) introducing recent advances in the application of this method, thanks to abundant, high-quality data sets recorded by a dense seismic network deployed in the study area during the Atarfe-Santa Fe seismic series (2020–2021). We also determined high-resolution P- and S- wave tomography for 3-D isotropy of the study area down to 14 km depth and then the three-dimensional distributions of Poisson's ratio (σ). The result for the uppermost crust reveals the lower velocities associated with the predominantly Neogene-Quaternary sediments in the Basin. During the Atarfe-Santa Fe seismic series there were five earthquakes with a magnitude of over 4.1. In the source areas of the first of these earthquakes, significant variations were detected in P-velocities and high Poisson's ratios. This suggests that fluids might be involved in the nucleation and development of the seismic sequence. The fast polarization directions (NE-SW) in the central study area are mostly parallel to the Cadiz-Alicante fault system and almost perpendicular to the NW-SE fault plane directions obtained from the focal mechanism solutions for the earthquakes with the largest magnitudes, which present a clearly NE-SW extensional model. At the end of the middle Miocene, the Cadiz-Alicante fault system was practically immobilized, and an approximate NNW-SSE compression with a perpendicular extension, which was strongly pronounced in the Granada basin, was established. This extension is now active. Our results could therefore be suggesting that extension tectonics is the dominant effect in the upper crustal depth, as reflected by a significant NE-SW Fast Velocity Direction (FVD). Another possibility is that the FVD may have continued unchanged since the end of the middle Miocene due to the control exerted by the Cadiz-Alicante fault system, indicating structure-induced crustal anisotropy.

## 1. Introduction

Sedimentary basins usually amplify and elongate ground motions when traversed by seismic waves at seismic frequencies at which urban infrastructure resonates. High-resolution characterization of the seismic structure beneath a sedimentary basin is therefore essential to make reliable predictions of ground motions, which are vital for mitigating seismic hazard. However, even when we have information on the seismic structure it is very difficult to characterize a sedimentary basin without having a very detailed knowledge of its anisotropic structure. Another important issue is that the origin of seismic anisotropy and its relation to the tectonic characteristics of a region are currently a subject of debate. In 1990, Kaneshima found at least three phenomena explaining the origin of shear-wave splitting: (1) vertically or subvertically aligned stress-induced microcracks, (2) cracks or fractures located in the vicinity of active faults that were oriented parallel to the fault planes and (3) an intrinsic rock anisotropy resulting from preferred mineral orientations. A detailed anisotropy study near the San Andreas fault trace at Parkfield was conducted by Daley and McEvilly (1990), who suggested that anisotropy may be caused by the fabric of the fault zone. Several researchers [Babuska and Cara, 1991; Crampin, 1994] cite regular patterns of tectonic fabric, stress-aligned microcracks, and preferred mineral alignment as explanations for the seismic anisotropy observed in crustal studies.

* Corresponding author.
*E-mail addresses:* inmasb@ugr.es (I. Serrano), madengra@ugr.es (M.A. Dengra), ftormed@upo.es (F. Torcal), zhao@tohoku.ac.jp (D. Zhao).

https://doi.org/10.1016/j.tecto.2024.230360
Received 14 November 2023; Received in revised form 20 May 2024; Accepted 21 May 2024
Available online 23 May 2024

If we look at studies of sedimentary basins, Liang et al. (2020) reported, in a study of the Sichuan basin (China), that the Fast Polarization Directions (FPDs) of shear waves are dominantly perpendicular to the edges of the basin and the FPDs inside the Sichuan basin are quite different between the two shallowest depths. The latter could suggest that the sedimentary layers and crystalline basements have different responses to regional stresses. These authors concluded that the different tectonic processes may lead to different angular differences between the FPDs and the GPS velocity. Both the GPS velocity and the FPDs of anisotropies are related to regional tectonic stresses. In some regions, the flow of materials results in the alignment of planar or linear structures, such as rock layers, fault fabrics and elongated rocks, in the direction of the flow. The surface wave traveling in this direction travels preferentially in the fastest layer/column. In this case, the FPDs are parallel or subparallel to the GPS velocity directions. For their part, in an analysis of ambient-noise-derived Rayleigh waves, Schippkus et al. (2020) found that the seismic anisotropy in the Vienna Basin area in the topmost kilometers of the crust is apparently controlled by the regional stress field, via crack-induced anisotropy. This was corroborated by the active faults in the area whose orientation closely matched that of the stress field. At deeper levels in the crust, anisotropy was controlled to some extent by crystal alignment due to deformation caused by faults and lateral extrusion in the area. The orientations were closely in line with what might be expected from the deformation. In one of the latest studies published on P-wave anisotropy, Liu et al. (2022) concluded that the northern Slaton Trough basin is dominated by NW-SE Fast Velocity Directions (FVDs), which could be due to the active compression happening in this area. By contrast, the southern Salton Trough basin is dominated by *E*-W oriented FVDs, possibly due to faulting and/or block rotation.

Despite the inherent complexity of interpreting seismic anisotropy and the difficulties involved in unraveling its origin, in this research we attempt to characterize the upper crust of the Granada Basin from the results of high-resolution seismic anisotropic tomography obtained from the inversion of the arrival times of local earthquakes. The availability of a dense seismic network in this area has allowed us to collect high-quality data from many earthquakes of small magnitude, and in particular from the Atarfe-Santa Fe seismic series (Informe, 2021).

Many researchers have investigated the seismic structure of the Granada Basin and these studies have greatly improved our understanding of the seismicity and seismotectonics of this region (Galindo-Zaldívar et al., 2015; Stich et al., 2010a, 2010b; Sanz de Galdeano, 2020; Madarieta-Txurruka et al., 2021, 2022; Lozano et al., 2022). The Granada Basin is a Neogene-Quaternary intramountain basin within the Betic Cordillera (SE Spain). According to Sanz de Galdeano et al. (2012), this basin is affected by many faults that can be grouped together into three sets: (1) the first set consists of the faults in an N60E to *E*-W direction, which are the longest and oldest; (2) the second set covers the NNE-SSW faults, which are very important, especially to the east of the cordillera; and (3) the third set is made up of faults running approximate NW-SE, which are also present in the eastern sector and inner regions of the basin, affecting areas such as Sierra Elvira, Granada, Padul, etc. Numerous studies describe these NW-SE active normal faults (Rodríguez-Fernández and de Galdeano, 2006; Sanz de Galdeano, 2020; etc.) whose NE–SW regional extension was confirmed by determining the moment tensor (Stich et al., 2006; Stich et al., 2010a) and focal mechanism solutions (Galindo-Zaldívar et al., 1999). A large part of the seismicity in this area has been attributed to these NW-SE normal faults (Madarieta-Txurruka et al., 2021, etc.). Most recently, Martin-Rojas et al. (2023) quantified short-term fault slip rates in the Granada Fault System ($0.9 \pm 0.3$ mm/year) on the basis of GNSS-derived geodetic data.

The Granada Basin has experienced some of the most devastating earthquakes in the history of the Iberian Peninsula (Vidal, 1986) and remains one of its most active seismic areas in terms of both the number and the magnitude of these events. A very striking feature of the region is that it is often struck by a series of earthquakes, the last of which occurred in 2020–2021. This sequence was felt over much of the city of Granada and its surrounding metropolitan area and the largest earthquake had a magnitude of mbLg 4.6 (Informe, 2021). The seismicity and current stresses highlighted by earthquake focal mechanisms reveal the activity of the NE-SW extensional system in the shallowest 12 km of the Granada Basin.

The first stage in this study was to estimate the three-dimensional P- and S-wave seismic velocity distribution and anisotropy beneath the Granada Basin. We then compared this distribution with the results obtained using various different geophysical methods, and studied the implications this could have for our understanding of the structure and dynamics of the Basin. We also wanted to provide a detailed assessment of the relationship between the seismic and tectonic characteristics, and of the local deformation in the upper crust. Although several models of the study area have been obtained from local seismic tomography (Dañobeitia et al., 1998; Calvert et al., 2000; Gurria and Mezcua, 2000; Serrano et al., 2002), they all involve isotropic velocity tomography, in which the Earth's structure is assumed to be isotropic for the propagation of seismic waves. According to Zhao et al. (2023), this is because in many cases the seismic data sets used in tomography do not have enough data and/or ray-path coverage to resolve the anisotropic part of the signal. Seismic anisotropy can cause the largest changes in seismic velocities, perhaps even greater than those caused by changes in temperature, composition, or mineralogy. With this in mind, the main objective of this study was to take advantage of the magnificent seismic ray coverage provided by the Atarfe-Santa Fe seismic series (2020–2021) to obtain a three-dimensional distribution of seismic anisotropy below the study area. In addition, our study seeks to highlight the importance of analyzing the seismic anisotropy in sedimentary basins when trying to predict the ground motion of future earthquakes, given that at present, anisotropy models are rarely used in physics-based ground motion prediction.

## 2. Data and methodology

Seismic tomography is one of the most important geophysical techniques for determining the three-dimensional (3D) distribution of the physical properties inside the Earth that affect seismic-wave propagation. These properties include elastic, anelastic, and anisotropic parameters, as well as material density (Thurber and Ritsema, 2015). Seismic anisotropy tomography is an updated geophysical imaging technology that can display 3D variations in both structural heterogeneity and seismic anisotropy, providing unique insights into geodynamic processes in the Earth's crust and mantle (Zhao et al., 2023).

The region studied covers an area of 2164 $km^2$ (Fig. 1) in which each earthquake has been recorded by at least 5 seismic stations. The selected time period was from January 2010 to March 2022. The initial datasets were obtained from the catalogs produced by the Andalusian Institute of Geophysics (IAG, UGR) of the University of Granada (UGR), who monitor the Andalusian Seismic Network (RSA), and from those produced by the National Geographic Institute (IGN), who manage the National Seismic Network (RSN). Most of the earthquake arrival time data came from 30 seismic stations within the study area, although 34 additional seismic stations outside the study area were also used.

To choose the most suitable database for the inversion, we compared the set of original RSA and RSN locations for the same time period, spatial volume and velocity model adapted to the Betic Cordilleras (table S1). In the initial database many more earthquakes and seismic phases were obtained from the RSA than from the RSN (7051 earthquakes including 96,896 P- and S-phases from the RSA versus 3913 earthquakes containing 51,405 P- and S-phases from the RSN). The dataset with the best fit between P- and S-wave arrival times (0.99) was RSA. The initial travel time residuals for the RSA database were 0.21 s. and 0.17 s. for P- and S-waves respectively, while for the IGN database they were 0.36 s. (P-waves) and 0.39 s (S-waves).

A total of 7051 earthquakes, which included 63,909 P-phases and

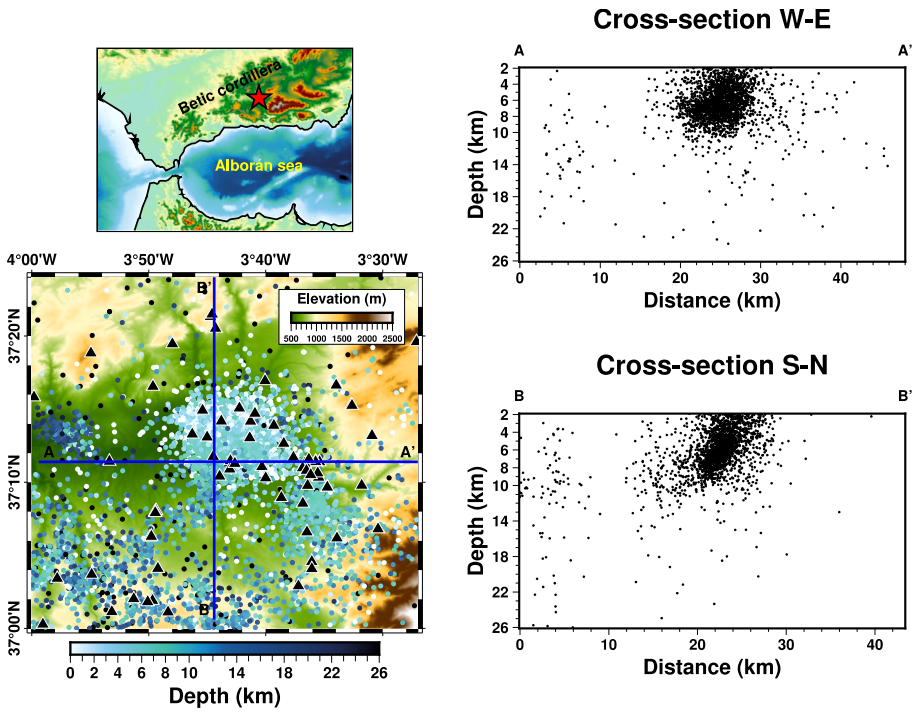


**Fig. 1.** The top-left image shows the geographical situation of the study area (red star) while the one on the bottom left shows the distribution of the 7051 earthquakes (colored dots) and seismic stations (black triangles) used in this study. The different colors indicate the focal depth according to the scale at the bottom of the map. The blue lines running N-S and W-E mark the locations of the vertical cross-sections displayed in the images on the right, which illustrate the distribution of seismicity in depth. (For interpretation of the references to colour in this figure legend, the reader is referred to the web version of this article.)

32,987 S-phases, were selected for the initial database. The database was then relocated using an iterative least squares method [Zhao et al., 1992] with three different velocity models A, B and C (Table S2). The first model came from the initial velocity model used by the IAG (UGR) in the location routine, the second model was similar to the model used by the IGN, and the third model was based on the results obtained by Serrano et al. (2002) in the same area. The reliability of the different velocity models used in the seismic inversions was then assessed and the results can be seen in Table S3.

The seismic tomography method proposed by Zhao et al. [1992] was applied to the selected dataset. A three-dimensional grid net was set up in the modeling space. Perturbations to the velocities at the grid nodes and hypocentral locations were taken as unknown parameters. Travel times and ray paths were calculated using a 3-D ray-tracing technique. The LSQR algorithm of Paige and Saunders (1982) was used for inversion. The nonlinear tomographic problem was solved by iteratively conducting linear inversion. The tomographic method is explained in greater detail in Zhao et al. (1992).

For model A, after three iterations, the average uncertainty of their origin times was reduced from 0.33 s. to 0.16 s (Table S3). After relocation of the earthquakes, the root-mean-square (RMS) travel-time residual was reduced from 0.26 s. to 0.22 s. for P-wave arrivals and from 0.27 s. to 0.23 s. for S-wave arrivals. The results for models A, B and C are shown in Table S3. On the basis of these results, it is difficult to reach a conclusion as to which model is best, in that while the results for models A and C are slightly better than for model B, the latter has a substantially higher number of reconstructed nodes. In the end we chose velocity model A, because it had a larger total number of seismic phases than the other two models and lower average uncertainty of the origin times after three iterations.

Three inversions were performed with different parameterization models to obtain the best possible resolution. The inversions were run with a distance between grid nodes of 0.01°x 0.01°, 0.02° x 0.02° and 0.03° x 0.03° (latitude x longitude respectively). The spacing finally selected was 0.02° x 0.02° (≈2.2 km x ≈ 2.2 km). In all cases, inversions were conducted at depths of 2, 4, 6, 8, 10, 14, 18, 22 and 26 km. The number of nodes in the modeled space was 22 × 30 × 9 (latitude, longitude, depth), making a total of 5940.

For model A we solved the inverse problem with 10,413 velocity parameters (5039 for Vp and 5374 for Vs) at the grid nodes with hit counts (i.e., the number of rays passing through each grid node) >10. The results for the three models are shown in Table S3.

Once we had selected the network space, we then repeated a number of inversions using different damping and smoothing values. Smoothing and damping regularizations were applied to eliminate dramatic short-scale variations in the unknown parameters (Zhao, 2009). The reduction in the travel time residual was then compared to the variance in the solutions and a tradeoff curve was drawn between the two. The value selected as the damping parameter for the entire dataset was the one that gave optimum residual reduction and solution variance (Fig. S1). The same method was applied for the smoothing parameter.

After obtaining the P- and S- wave velocity distribution, the elastic parameter Poisson's ratio (σ) was calculated using the formula $(V_p/V_s)^2 = 2(1 - \sigma)/(1 - 2\sigma)$ (see Utsu, 1984). Poisson's ratio, which can be a helpful indicator of lithology and pore fluid pressure, is directly correlated with Vp/Vs, the ratio of compressional and shear-wave velocities. For the crust and upper mantle of Earth, the average Poisson's ratio is 0.25 (Holbrook, 1988). Any deviation from this value could indicate a change in the characteristics of the rock in these areas. In common rock types, the Poisson's ratio ranges from 0.20 to 0.35 (Christensen, 1996). Poisson's ratio has also proved very effective in the clarification of the seismogenic behavior of the crust, and in particular in the role of crustal fluids in the nucleation and growth of earthquake rupture (e.g. Zhao et al., 2002).

To study the 3-D P-wave azimuthal anisotropy below the Granada Basin, we applied the anisotropic tomography method proposed by Wang and Zhao (2013). This procedure was developed from the isotropic tomography method designed by Zhao et al. (1992) and uses an anisotropy method similar to that of Eberhart-Phillips and Henderson (2004). Wang & Zhao's method extends the technique developed by

Hearn (1996) by implementing azimuthal anisotropy in a simultaneous inversion for 3-D seismic velocity and hypocenters. They added two anisotropic parameters at each velocity node, applying the following equation (Backus, 1965; Raitt et al., 1969) to characterize weak azimuthal anisotropy for P waves:

$$S(\varnothing) = S_0 + Acos(2\varnothing) + Bsin(2\varnothing) \quad (1)$$

where $S$ is the anisotropic slowness, $S_0$ is the azimuthal average slowness (i.e. isotropic component), $\varnothing$ is the ray path azimuth and $A$ and $B$ are the anisotropy parameters. The fast velocity direction (FVD, or anisotropic azimuth) is expressed as follows:

$$\psi = \frac{1}{2}tan^{-1}\left(\frac{B}{A}\right) + \begin{cases} \pi/2, \mathrm{A} > 0 \\ 0, \mathrm{A} < 0 \end{cases}$$

The magnitude of the anisotropy can be described in terms of the A and B values shown in eq. 1 or in terms of the fast direction and the total anisotropy, M, or the percentage of anisotropy, α.

$$M = \sqrt{A^2 + B^2}$$

$$\alpha = \frac{V_f - V_s}{V_0} = \frac{2M}{S_0 - M^2/S_0}$$

where $V_f$ and $V_s$ are the velocities in the fast and slow directions.

In line with this approach, we applied the tomographic method for azimuthal Vp anisotropy (Wang and Zhao, 2008, 2013). Horizontal hexagonal symmetry was assumed in the modeled space and two anisotropic parameters (A and B) were defined at each node of the network along with isotropic Vp parameters.

A 3D network was then created with different node spacings of 0.01° x 0.01°, 0.02° x 0.02° and 0.03° x 0.03° (latitude x longitude respectively). In the end, to express the 3-D azimuthal anisotropy, we selected a spacing of 0.02° x 0.02° and a vertical grid interval of 2 km (the same parameters used in isotropic tomography). The same initial velocity and damping model was used as in isotropic tomography, although the smoothing was set at 10/100 as compared to 100/100 for the isotropic inversion. The final number of nodes in the three dimensions was 22 × 30 × 9 (latitude, longitude, depth), which when multiplied together made a total of 5940.

We solved the inverse problem with 63,909 velocity parameters for Vp at the grid nodes with hit counts of >10 for model A (Fig. S2). The results for models A, B and C can be seen in Table S4.

According to Huang et al. (2015), when only a narrow ray azimuthal range is available, the inverted isotropic Vp anomalies and the azimuthal anisotropy could be strongly associated. They could also be strengthened or weakened depending on the directions of the rays used. These effects (including smearing, strengthening, and weakening) are also visible when the ray azimuthal range is 60°. However, they are significantly improved when the azimuthal range reaches 90°. The isotropic Vp anomalies and the azimuthal anisotropy are mostly restored independently when the ray range is 120° or greater. Table S4 shows that 3676 nodes with a ray azimuthal range of over 60° were used.

In the same way as we had done earlier with seismic isotropy, we repeated various inversions with different damping and smoothing values. The values chosen for the damping and smoothing parameters were those that provided optimum residual reduction and solution variance.

## 3. Checkerboard resolution test

When studying the concept of resolution here, our aim was to find out how the real Earth is reconstructed in the calculated image. Several methods were used to determine whether or not the inversion results were sufficiently reliable for interpretation purposes. In this research, the stability and resolution of the results were qualitatively assessed by the Checkerboard Resolution Test (CRT), so as to test the resolution of the tomography model by making a synthetic velocity model (Fig. 2). Positive and negative velocity perturbations of ±3% were assigned to all the 3D grid nodes, after which synthetic travel times were calculated for the checkerboard model. The same numbers of events, stations and ray paths were used as in the real tomographic inversion. We also added random errors with a normal distribution with a standard deviation of 0.05 s (Fig. 2) and 0.10 s (Fig. S3) to the synthetic data to simulate the picking errors in the observed arrival-time data. We then inverted the synthetic data using the same algorithm as for the real data. This method was applied in Grand (1987) and the basic idea for the test came from Humphreys and Clayton (1988). For the azimuthal tomography in the input model, FVDs that were perpendicular to each other (22.5° and 112.5°) and had an anisotropy amplitude of 3% were introduced at two adjacent nodes. In Fig. 3 and Fig. S4, the red and blue bars indicate the initial and final synthetic model, respectively. In the same way as in the previous tests, random errors in a standard distribution of 0.05 s and 0.10 s were added to the theoretical arrival times for the CRT input models. The Checkboard Resolution Test was used to assess the resolution of the result.

As expected, the recovered images show that at shallow depths (≤ 10 km) model recovery is mainly affected by the distribution of local earthquakes and the input model is recovered very well in the central part of the study area. The more local events in any given area, the better the recovery. At greater depths, the results are less reliable. As a whole, the test results indicate that the input checkerboard model can be recovered well for both the isotropic Vp structure and azimuthal anisotropy in shallower layers of the crust in the central part of the study area.

## 4. Results and interpretation

### 4.1. Seismic images from the isotropic velocity model

One of the most significant results in the first 2 km layer (Fig. 4) is the large negative Vp anomaly, which in some places reaches values of −6% compared to the initial velocity model, as well as the strong positive velocity anomaly extending from Sierra Elvira southwards. The Granada, Cubillas and Chimeneas depocenters (GR, EC-WC and CH in Fig. 4) are obtained from seismic inversion as low seismic velocity areas. The high gravity values in Sierra Elvira (SE) coincide with the important positive Vp values, reaching almost 4%, extending to the SW in the 2 km and 4 km depth layers. The parallel faults in the SW boundary of Sierra Elvira, Atarfe (AT) and Pinos Puente (PP) are located in this high Vp anomaly. At 4 km depth, the hypocenters of the five earthquakes with a magnitude of over 4.1 in the Atarfe-Santa Fe seismic series (2020–2021) and a depth from 3 to 5 km (Informe (2021)) coincide with a change in the distribution of Vp from high to low velocities. The Santa Fé fault (ST) runs parallel to the previous ones and its superficial trace crosses high Vp zones to the NW and low Vp zones to the SE at a depth of 2 km. While at 4 km depth its surface trace crosses almost entirely low velocity zones, at 2 km depth the Poisson's ratio results (Fig. 5) show that the northwestern fault sector is located in a low rigidity area (high σ) coinciding with the hypocenters of major earthquakes, while the southeastern part of the fault is bounded by a block of high rigidity (low σ). At 4 km depth, the Poisson's ratio has a similar distribution. In general, the seismogenetic area of the Atarfe-Santa Fe series shows high Poisson's ratio values in the 2–4 km layers. At 6 km depth, however, the Poisson's ratio values are much lower in the same area below the hypocentral zone. Fig. 6 shows that the hypocentral area of the first, shallowest earthquake is located in a high σ area between 1 and 5 km depth. However, below 5 km depth, where the rest of the earthquake is located, the Poisson coefficient is lower than in the shallower layers. Figs. S5 (P- wave) and S6 (S- wave) show the results of a checkerboard resolution test along the profile shown in the inset map of the Fig. 6.

When it comes to interpreting the results, it is important to bear in mind that the velocity at a particular point in the grid represents the best

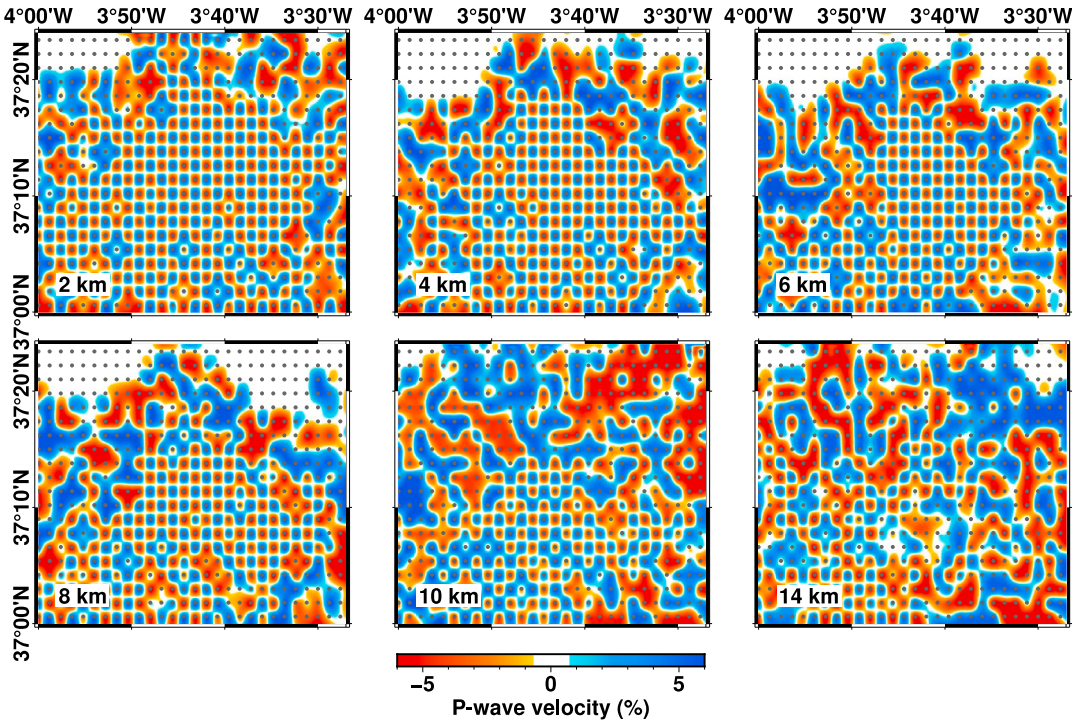


**Fig. 2.** Results of a checkerboard resolution test for Vp tomography. The red and blue squares indicate slow and fast velocities, respectively. The depth of each layer is shown in the bottom-left corner of each map. The grid interval is 0.02° in the horizontal direction and 2 km in depth. The Vp perturbation scale is shown at the bottom. Random errors with a standard deviation of 0.05 s for P-wave were added to the travel times calculated from the synthetic model. (For interpretation of the references to colour in this figure legend, the reader is referred to the web version of this article.)

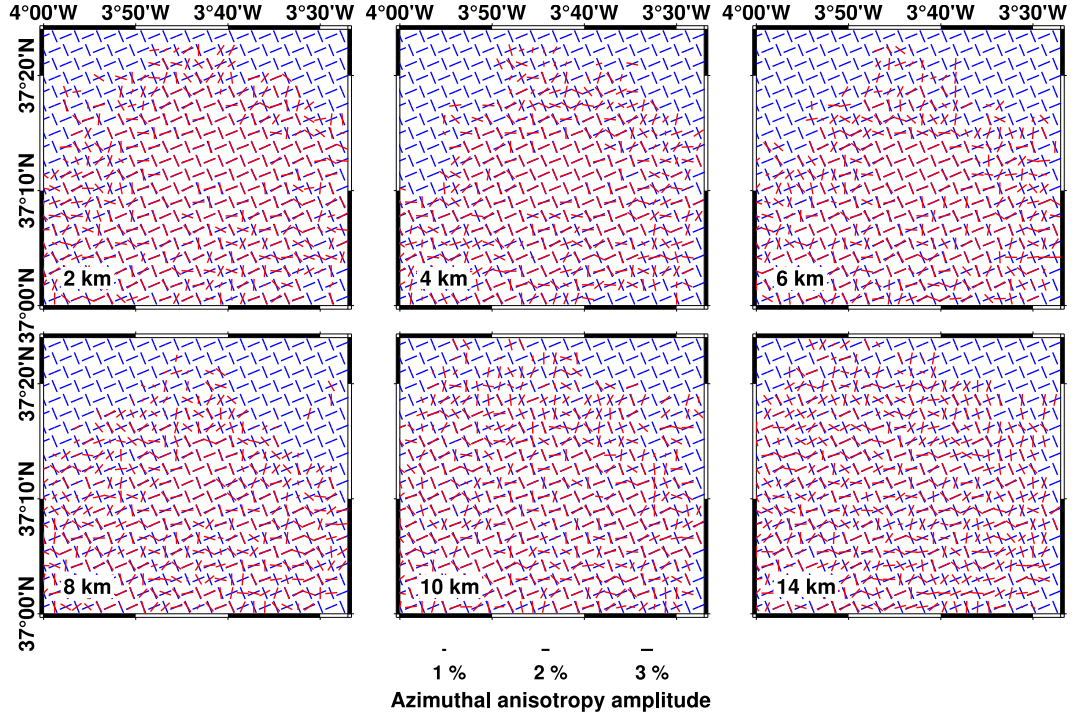


**Fig. 3.** Map views showing the results of a checkerboard resolution test for Vp azimuthal anisotropy tomography. The layer depth is shown in the bottom-left corner of each map. The FVDs at two adjacent grid nodes are perpendicular to each other (22.5° and 112.5°) with an anisotropy amplitude of 3.0%. The thin red bars show the fast velocity directions (FVDs) in the input model, while the blue bars indicate the FVDs recovered after the tomographic inversion. Random errors in a normal distribution with a standard deviation of 0.05 s were added to the theoretical arrival times calculated for the CRT input model. (For interpretation of the references to colour in this figure legend, the reader is referred to the web version of this article.)

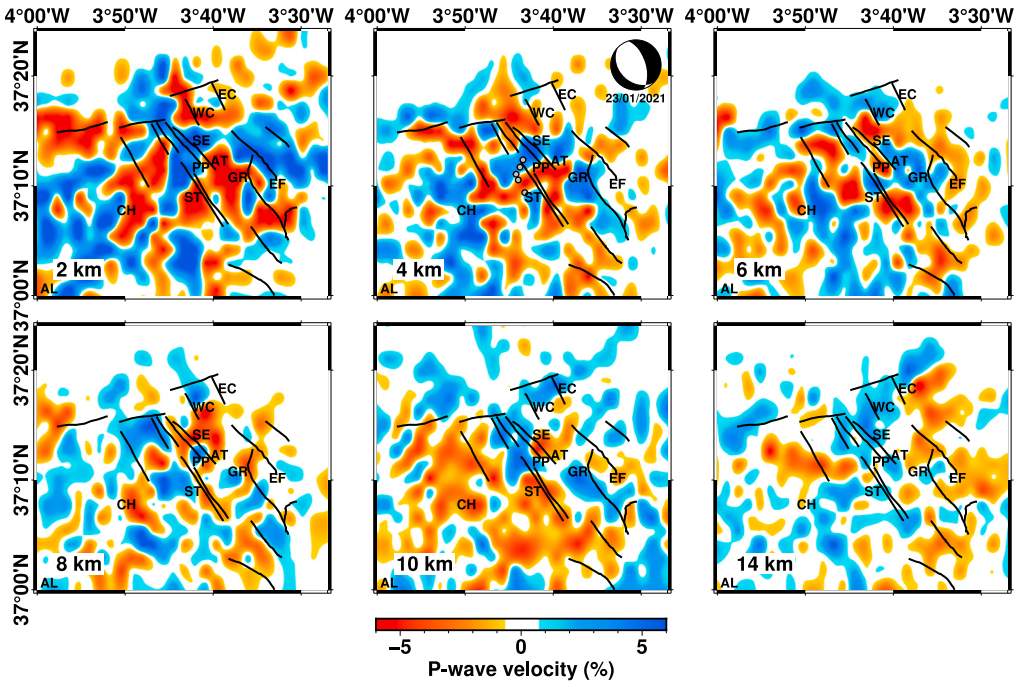


**Fig. 4.** Fractional Vp perturbations (in percentage) at six depth layers obtained from the database (model A). The Vp perturbation is calculated from the mean value of the inverted velocity at each depth. The red and blue colors indicate slow and fast velocities, respectively. The Vp perturbation scale is shown at the bottom. The grey circles indicate the epicenters of the five largest earthquakes in the Atarfe-Santa Fe seismic series (Informe, 2021). In the top-right corner of the second image, we can see the focal mechanism solution for the largest earthquakes recorded in January 2021, as computed by the Spanish IGN (Informe, 2021). The black line indicates the faults according to Sanz de Galdeano et al. (2003). Those cited in the text are referred to with the following abbreviations: GR: Granada fault, EC: East Cubilla fault, WC: West Cubilla fault, CH: Chimeneas, SE: Sierra Elvira, AT: Atarfe fault, PP: Pinos Puente fault, ST: Santa Fe fault and EF: El Fargue-Jun fault. (For interpretation of the references to colour in this figure legend, the reader is referred to the web version of this article.)

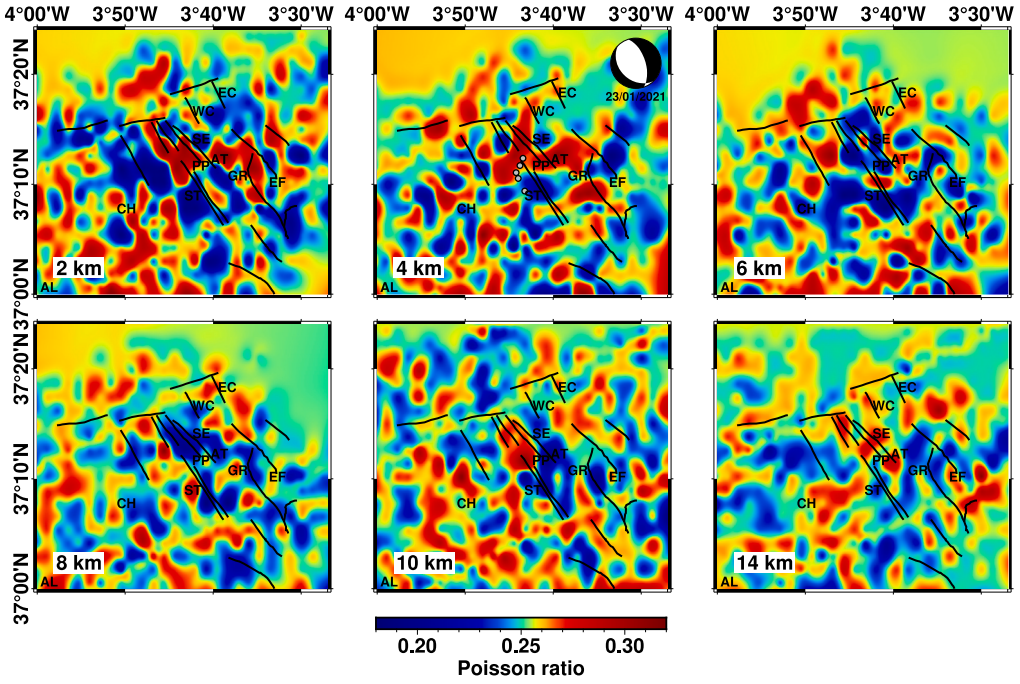


**Fig. 5.** Poisson's ratio at the six depth layers. The depth of each layer is shown in the bottom-left corner of each map. The blue and red colors denote low and high Poisson's ratios, respectively. The scale is shown at the bottom of the figure. See Fig. 4 for further details. (For interpretation of the references to colour in this figure legend, the reader is referred to the web version of this article.)

estimate for the volume surrounding that point. Similarly, the size and shape of velocity anomalies can provide reasonable estimates but may not correspond to the exact boundaries of true velocity features (Eberhart-Phillips, 1986). The comparison of seismic velocities using seismic tomography with gravity anomalies has long been a reliable method for identifying sedimentary fills in an intramountain basin like

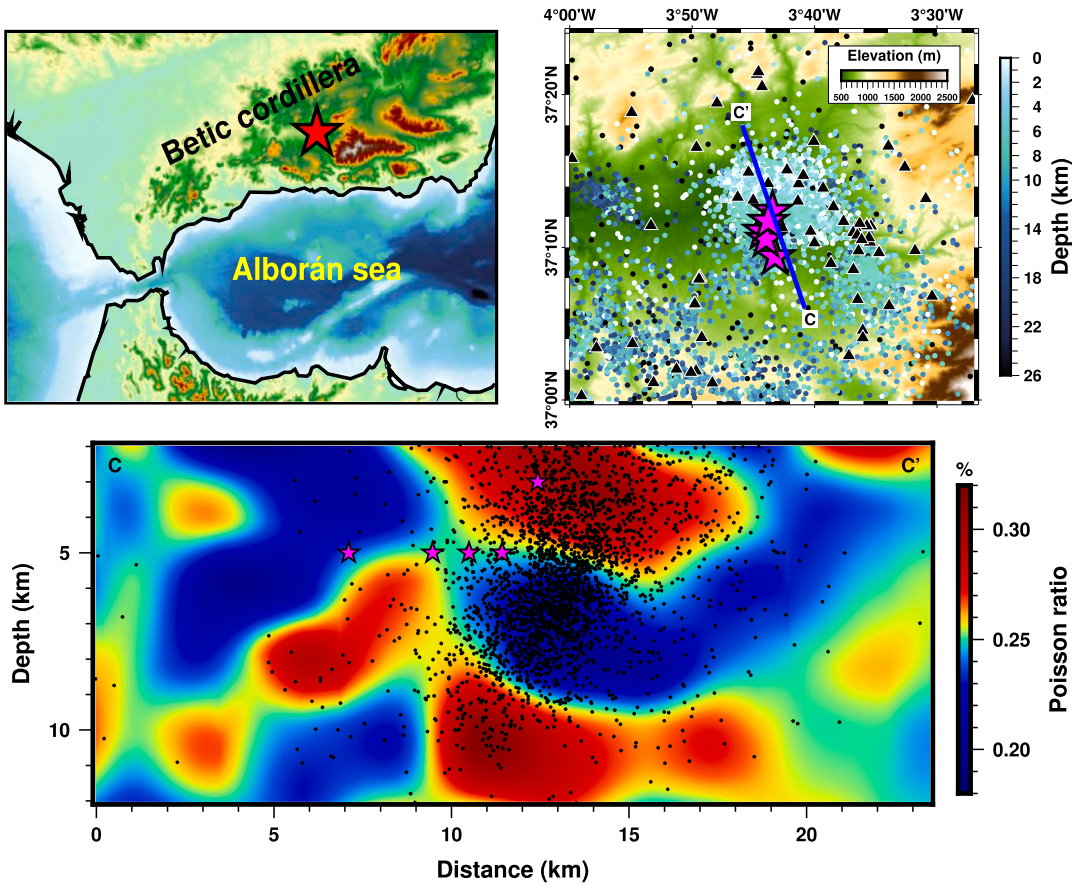


**Fig. 6.** The top-left image shows the geographical situation of the study area (red star). In the top-right image, the blue lines running NW-SE mark the location of the vertical cross-sections displayed at the bottom of the map, which illustrate the distribution of Poisson's ratio in depth. The pink stars show the locations of the five earthquakes with a magnitude >4.1 in the Atarfe-Santa Fe seismic series (2020–2021). (For interpretation of the references to colour in this figure legend, the reader is referred to the web version of this article.)

the Granada Basin. Due to its lower seismic velocities and lower density, it is possible to distinguish the sedimentary fill from the bedrock. In this way, it highlights both minimum anomalies, which are used to estimate the geometry of the bedrock. The presence of faults at depth causes abrupt variations in the thickness of the sedimentary infill and can therefore be identified in the high-resolution seismic images and gravity maps. The large negative Vp anomaly obtained at 2 km depth can be interpreted as the Neogene and Quaternary fills in the Granada Basin. According to the recent study by Madarieta-Txurruka et al. (2022), the Complete Bouguer Anomaly map shows a minimum in the Granada Basin. The values increase towards the north and the south, reaching a maximum in the southern part of the study area. This regional increase in the Complete Bouguer Anomaly values is due to long-wavelength anomalies, and is therefore, probably related to crustal thickness. However, the residual gravity anomaly map offers a better picture of the basin structure, which coincides in general with our results at shallow layers.

As mentioned earlier, the hypocentral area of the first, shallowest earthquake with a magnitude of over 4.1 (23/01/2021, 4.4 Mw, 3.0 km depth) is located in a high σ area between 1 and 5 km depth (Fig. 6). This indicates low stiffness of the materials and that fluids may be present. These fluids could be involved in the nucleation and development of the seismic sequence as this is the first, shallowest earthquake at the beginning of this series. Indeed, similar values of σ have been associated with high pore fluid pressure and fluid migration along active normal fault systems. Below 5 km depth, where the rest of the earthquakes with magnitudes of over 4.1 Mw are located, the Poisson coefficient is lower than in the shallower layers. This does not prevent the triggering of earthquakes in that seismicity can spread along multiple fault planes in different material states. Lozano et al. (2022) suggest that the Santa Fe fault may dip vertically with the steepest plane in the first 2–3 km, approximately, and then change to a more normal dipping angle below this depth, and that the seismicity is triggered along multiple parallel subsidiary faults that branch off from the main parent fault rather than along just one main fault.

On the south-western and south-eastern edges of the study area (Fig. 5), the Poisson's ratio values are low, indicating that the materials surrounding the Sierra Elvira block are more compact. At 6 km depth, however, the σ values are much lower in the same area. These values indicate an abrupt change in the properties of the materials at 4 and 6 km depth, which could be interpreted as alternating high and low stiffness in adjacent blocks.

As suggested by Zhao et al. (2002), lithological variations in the crust could lead to heterogeneities in the properties of the materials at a local scale and variations in stress distribution, in this way causing a weakening of the fault. The presence of high Poisson's ratios and strong seismic velocity contrasts suggest that the active faults in our region are mechanically weak and unstable, which could imply a high seismic risk in the Granada Basin. Assuming that this seismic contrast is one of the main characteristics of the study area, it could also imply that stress has accumulated in an existing fault zone with lateral heterogeneity in velocity. In addition, most of the microearthquakes in the Atarfe-Santa Fe seismic series were located in the upper crust zone between 2 and 10 km, which suggests that the base of the seismogenetic zone may be at a depth of 10 km. So, given that the material in the shallow crust is highly heterogeneous and the lithostatic pressure is low, initiation of the failure

probably ceases before an impending strong earthquake, causing numerous weak earthquakes to occur instead (Mori and Abercrombie, 1997).

Even though in our explanation and interpretation above, we only used the results of velocity model A, some of the seismic images obtained using the other models are nonetheless intriguing and worth analyzing. If we look at the results at the 2 km layer depth of the seismic isotropic inversion with velocity model B without relocating the earthquakes, some general geological and tectonic characteristics of the basin are more significant than with model A. For example, according to Sanz de Galdeano et al. (2003), the East Cubilla fault (EC) identified in seismic profiles affects the Plio-Quaternary materials. If we look at Fig. 7, this tectonic feature is situated between high and low velocities in the NNE of the basin, as reflected in the change in velocity between the basin fill and the bedrock. This would situate the edge of the basin at its NNE end. The El Fargue-Jun fault (EF) showed clear activity during the Quaternary and has been associated with the June 1998 seismic series. Our results suggest that it has similar characteristics to the previous fault, forming the eastern boundary of the basin. This confirms the suitability of the velocity model we selected (model A), which is better adapted to the characteristics of the study area in that it includes the extensive sedimentary fill, a defining feature of the basin.

### 4.2. Seismic images and anisotropy from the anisotropic velocity model

In the isotropic inversion, the effects of the azimuthal anisotropic model are mapped onto the isotropic Vp image. The lack of homogeneity in the angular coverage of the ray paths can result in an apparent anisotropy (Ishise et al., 2012). In the azimuthal inversion, the contributions made by seismic anisotropy to the travel-time residuals are, at least partially, independent of the isotropic Vp image. As a result, the three isotropic Vp models display certain differences in the amplitude and spatial extent of the Vp anomalies. These differences in the isotropic Vp image may indicate that seismic anisotropy has a greater impact on the structure of the study area.

Our results for the anisotropic model (Fig. 8) show large variations and strong contrasts in the FVDs and in the magnitude of the anisotropy at different depths. The maximum anisotropy in the uppermost crust was approximately 3%. The high velocity area of Sierra Elvira (SE) and its extension south-southwards show a well-defined NE-SW FVD to 10 km depth. It has by far the highest seismic anisotropy in the region, more than doubling the results for the rest of the study area. This is the most striking and significant result of the whole anisotropic inversion. Towards the depocentre of Granada (GR), the FVD turns slightly NEE-SWW. By contrast, the south-western sector of the central basin (CH) shows a preferential NW-SE direction. From 2 km - 10 km depth, the fast axes of the azimuthal anisotropy hardly change direction.

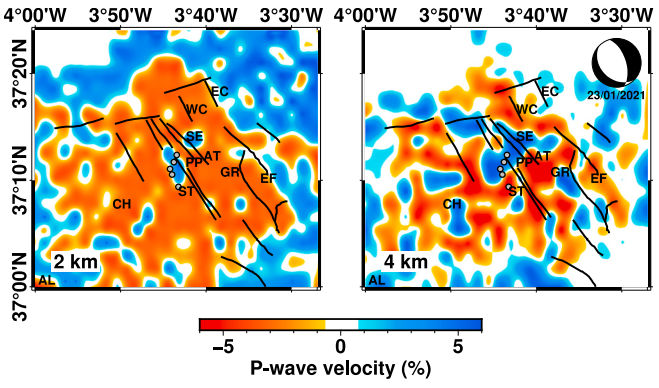


**Fig. 7.** Fractional Vp perturbations (in %) at two depth layers (2 and 4 km depth) obtained from the database from model B. The Vp perturbation is from the mean value of the inverted velocity at each depth. The red and blue colors indicate slow and fast velocities, respectively. The Vp perturbation scale is shown at the bottom. See Fig. 4 for further details. (For interpretation of the references to colour in this figure legend, the reader is referred to the web version of this article.)

One interpretation of the azimuthal seismic anisotropy results is that the FVDs reflect the great diversity in the elements that control the distribution of stress in the Granada Basin.

The fast polarization directions (NE-SW) in Sierra Elvira (SE) and its extension south-southwards are mostly parallel or sub-parallel to the Cadiz-Alicante fault system and almost perpendicular to the NW-SE fault plane directions obtained from the solutions of the focal mechanisms for the earthquakes with the greatest magnitudes in the Atarfe-Santa Fe seismic series (Informe, 2021), which present a clear NE-SW extensional model. According to Sanz de Galdeano (2008), the Cadiz-Alicante fault system was practically immobilized at the end of the middle Miocene and an approximate NNW-SSE compression with a perpendicular extension, strongly pronounced in the Granada basin, was established in the Betic Cordillera. Our results could be suggesting that extension tectonics is the dominant effect in the upper crustal depth reflected by a significant NE-SW FVD.

Another possibility is that the FVD may have remained unchanged since the end of the middle Miocene due to the control exerted by the Cadiz-Alicante fault system, indicating structure-induced crustal anisotropy.

Independent data obtained from the horizontal CGPS (Continuous Global Positioning System) velocity field was presented in a recent paper by García-Armenteros (2023). The stations in the central sector of the Betic Cordillera present a higher southwestward component instead of the purely westward motion obtained in previous studies (Garate et al., 2015; Koulali et al., 2011). This new direction supports the conclusions of González-Castillo et al. (2015) that a clockwise block rotation is currently occurring in the northern branch of the Gibraltar Arc tectonic belt. According to new data presented in the study, this region is currently undergoing a northwest-southeast convergence with Nubia at a rate of 3.5 ± 0.1 mm/yr. The displacements as a whole also coincide with the tectonic model involving rollback and indentation tectonics in the Gibraltar Arc proposed by Galindo-Zaldivar et al. (2022). Our results also show that the azimuthal anisotropy pattern largely resembles the surface motion revealed by GPS, especially in the Sierra Elvira and its surrounding area.

However, the FVDs are subparallel to the major fault strikes in the Chimeneas area (CH). The checkerboard resolution test (Fig. 3) shows poor P-wave velocity resolution in layers at depths from 4 km to 14 km, and Fig. 8 shows that the only robust results are those for the first layer. For these reasons, we have decided not to interpret the seismic anisotropy results in the Chimeneas area (CH).

As regards the origin of seismic anisotropy, it could be caused by structures that have gradually been deformed over their long-term history. It could also be produced by the actual strain rate field, in the same way as the GPS velocity field represents an instantaneous response to tectonic forces. According to Madarieta-Txurruka et al. (2022), there is a striking discrepancy between the extension vectors calculated from the stress tensors of the focal mechanisms (<15 km) and the surface CGPS data. This could be due to a heterogeneous local uplift that raised basement blocks in the south of the basin, giving rise to gravity collapse processes and the rotation of the extensional axis at the surface.

The Granada Basin appears to be affected above all by two of the three fault systems described by Sanz de Galdeano et al. (2003) for the Betic Cordilleras, as reflected in the azimuthal anisotropy results. These are the faults running N70°E to *E*-W and those running in an NW-SE direction. In those areas where active fault zones do not show fault-parallel fast polarization directions, structure-induced crustal anisotropy should not exist.

The fact that in the first 10 km of the upper crust, the fast axes of the azimuthal anisotropy hardly change direction could indicate that the entire upper crust has the same deformation pattern. The anisotropic pattern in the study region can be divided into two parts: in the central

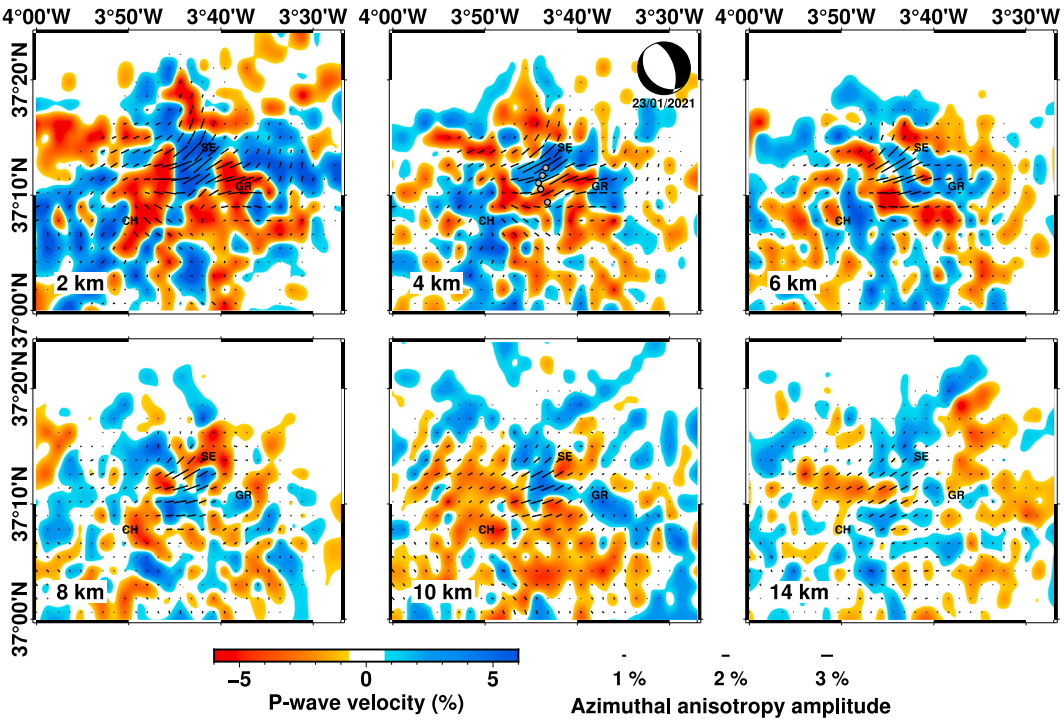


**Fig. 8.** Map views of Vp azimuthal anisotropy tomography. The layer depth is shown in the bottom-left corner of each map. The red and blue colors indicate low and high isotropic velocities, respectively. The orientation and length of the short black bars indicate the fast-velocity direction (FVD) and the anisotropic amplitude, respectively. The anisotropic amplitude scale is shown at the bottom. See Fig. 4 for further details. (For interpretation of the references to colour in this figure legend, the reader is referred to the web version of this article.)

sector the fast axes remain oriented almost NE-SW throughout the crust, while in the surrounding area there is a wider range of FVD solutions.

## 5. Conclusions

We obtained detailed three-dimensional P- and S-wave velocities and Poisson's ratio images together with P-wave azimuthal anisotropy in the upper crust beneath the Granada Basin. The dataset used in this study consists of 63,909 P- and 32,987 S-wave arrival times from 7051 local earthquakes recorded by seismic stations in the study area over the period 2010–2022. Numerous inversions were performed to evaluate how the seismic images were affected by a range of different factors (the initial data sets, modeled volume parameterization, damping and smoothing parameters) even when the same inversion algorithm was used. The impact of initial velocity models on final image reconstruction results was investigated using three different velocity models. The models selected at the end of this process were those that provided the best results in the checkerboard resolution test and the root mean square of the travel time residual.

Tomographic imaging of the uppermost crust revealed the lower velocities associated with the predominantly Neogene-Quaternary sediments in the Granada Basin. The most recent study of the residual gravity anomaly map (Madarieta-Txurruka et al., 2022) coincides in general with our results at shallow depths in that the most important depocenters obtained from seismic inversion are low seismic velocity areas. The high gravity values in Sierra Elvira are in line with the high positive Vp values, extending to the SW in the 2 km and 4 km depth layers. In the source areas of the largest earthquakes in the Atarfe-Santa Fe seismic series (Informe, 2021), tomographic imaging has detected significant velocity variations of up to ±6% in P velocities and high Poisson's ratio values. Of the 5 earthquakes with a magnitude of over 4.1 Mw, the first had a depth of 3.0 km and was located inside a high σ area (Fig. 6). This could indicate the presence of fluids and the low stiffness of the materials. This implies that fluids were probably involved in the triggering of the first, shallowest earthquake and by extension in the nucleation and development of the series as a whole. However, below 5 km depth, where the rest of the earthquakes with magnitudes of over 4.1 Mw are located, the σ is lower than in the shallower layers. This suggests greater rigidity of the material at these depths. However, this does not prevent the triggering of earthquakes, as seismicity can spread along multiple fault planes in different material states. According to Lozano et al. (2022) the Santa Fe fault may dip vertically with the steepest plane in the first 2–3 km, approximately, before changing to a more normal dipping angle below this depth. In this case, the seismicity would be triggered along multiple parallel subsidiary faults that branch off from the main parent fault rather than along just one single fault.

The presence of high Poisson's ratios and sharp contrasts in seismic velocity suggests that the active faults in this area are mechanically weak and unstable, making the Granada Basin an area of high seismic hazard.

The high velocity area of Sierra Elvira (SE) and its extension southwards show a well-defined NE-SW FVD to 10 km depth. It has by far the greatest seismic anisotropy values in the region, more than doubling the results for the rest of the study area. This is the most striking and significant result of the whole anisotropic inversion. These directions are mostly parallel or sub-parallel to the Cadiz-Alicante fault system and almost perpendicular to the NW-SE fault plane directions obtained from the focal mechanism solutions for the largest earthquakes in the Atarfe-Santa Fe seismic series (Informe, 2021), which present a clear NE-SW extensional model. According to Sanz de Galdeano (2008), the Cadiz-Alicante fault system was practically immobilized at the end of the middle Miocene and an approximate NNW-SSE compression with a perpendicular extension was established in the Betic Cordillera and was particularly pronounced in the Granada basin. Our results could imply that extension tectonics is the dominant effect in the topmost crustal depth, as reflected by a significant NE-SW FVD. Another possibility is that the FVD may have remained unchanged since the end of the middle Miocene due to the control exerted by the Cadiz-Alicante fault system,

indicating structure-induced crustal anisotropy.

In the uppermost crust of the central study area, the azimuthal anisotropy pattern largely resembles the surface motion revealed by GPS, especially in the Sierra Elvira area (SE) and it runs almost perpendicular to the strike of nearby major faults. From 2 to 10 km depth, there is virtually no change in the direction of the fast axes of the azimuthal anisotropy, which suggests that the whole of the upper crust is subject to the same deformation pattern. The anisotropic pattern in the study region can be divided into two parts: in the central sector the fast axes remain oriented almost NE-SW throughout the crust, while the surrounding area has a wider range of FVD solutions.

## CRediT authorship contribution statement

**I. Serrano:** Writing – original draft, Investigation, Data curation, Conceptualization. **M.A. Dengra:** Software, Methodology, Funding acquisition, Formal analysis, Data curation. **F. Torcal:** Supervision, Resources, Investigation, Conceptualization. **D. Zhao:** Software, Methodology, Investigation, Conceptualization.

## Declaration of competing interest

The authors declare that they have no known competing financial interests or personal relationships that could have appeared to influence the work reported in this paper.

## Data availability

Giving the data does not depend on my group, it is a decision of the research institute.

## Acknowledgements

This work has been funded by the following projects: “Visualización de modelos sísmicos temporales generados a partir de la integración de los tiempos de viaje de los terremotos registrados en Andalucía (Junta de Andalucía, P20_00694), PID2019-109608GB-100 from Spanish Research agency MCIN/AEI/ 10.13039/501100011033 and IMAG-MASEIS: PID2021-124381NB-C2 from Spanish Research agency MCIN/AEI. We would also like to thank Nigel Walkington for his thorough review of the English in this article.

## Appendix A. Supplementary data

Supplementary data to this article can be found online at https://doi.org/10.1016/j.tecto.2024.230360.

## References

Babuska, V., Cara, M., 1991. Seismic Anisotropy in the Earth. Modern Approaches in Geophysics. Springer Netherlands. https://books.google.es/books?id=uLbSTr3csBYC.

Backus, G.E., 1965. Possible forms of seismic anisotropy of the uppermost mantle under oceans. J. Geophys. Res. 70 (14), 3429–3439. https://doi.org/10.1029/JZ070i014p03429.

Calvert, A., Sandvol, E., Seber, D., Barazangi, M., Roecker, S., Mourabit, T., Vidal, F., Alguacil, G., Jabour, N., 2000. Geodynamic evolution of the lithosphere and upper mantle beneath the Alboran region of the western Mediterranean: constraints from travel time tomography. J. Geophys. Res. 105 (B5), 10871–10898. https://doi.org/10.1029/2000JB900024.

Christensen, N.I., 1996. Poisson’s ratio and crustal seismology. J. Geophys. Res. Solid Earth 101 (B2), 3139–3156.

Crampin, S., 1994. The fracture criticality of crustal rocks. Geophys. J. 118, 428–438.

Daley, T.M., McEvilly, T.V., 1990. Shear wave anisotropy in the Parkfield Varian well VSP. Bull. Seismol. Soc. Am. 80 (4) https://doi.org/10.1785/BSSA0800040857.

Dañobeitia, J.J., Sallarès, V., Gallart, J., 1998. Local earthquakes seismic tomography in the Betic Cordillera (southern Spain). Earth Planet. Sci. Lett. 160 (3–4), 225–239.

Eberhart-Phillips, D., 1986. Three-dimensional velocity structure in Northern California Coast Ranges from inversion of local earthquake arrival times. Bull. Seismol. Soc. Am. 76, 1025–1052.

Eberhart-Phillips, D., Henderson, C., 2004. Including anisotropy in 3-D velocity inversion and application to Marlborough, New Zealand. Geophys. J. Int. 156, 237–254.

Galindo-Zaldívar, J., Jabaloy, A., Serrano, I., Morales, J., González-Lodeiro, F., Torcal, F., 1999. Recent and present-day stresses in the Granada Basin (Betic Cordilleras): example of a late Miocene-present-day extensional basin in a convergent plate boundary. Tectonics 18 (4), 686–702. https://doi.org/10.1029/1999TC900016.

Galindo-Zaldívar, J., Gil, A., Sanz de Galdeano, C., Lacy, M., García-Armenteros, J., Ruano, P., et al., 2015. Active shallow extension in central and eastern Betic Cordillera from CGPS data. Tectonophysics 663, 290–301. https://doi.org/10.1016/j.tecto.2015.08.035.

Galindo-Zaldivar, J., et al., 2022. The Campo de Dalias GNSS Network Unveils the interaction between roll-back and indentation tectonics in the Gibraltar Arc. Sensors. https://doi.org/10.3390/s22062128.

Garate, J., Martin-Davila, J., Khazaradze, G., Echeverria, A., Asensio, E., Gil, A.J., et al., 2015. Topo-Iberia project: CGPS crustal velocity field in the Iberian Peninsula and Morocco. GPS Solutions 19 (2), 287–295. https://doi.org/10.1007/s10291-014-0387-3.

García-Armenteros, J.A., 2023. Topo-Iberia CGPS network: a new 3D crustal velocity field in the Iberian Peninsula and Morocco based on 11 years (2008–2019). GPS Solutions 27, 155. https://doi.org/10.1007/s10291-023-01484-8.

González-Castillo, L., Galindo-Zaldívar, J., de Lacy, M.C., Borque, M.J., Martinez-Moreno, F.J., García-Armenteros, J.A., Gil, A.J., 2015. Active rollback in the Gibraltar Arc: Evidences from CGPS data in the western Betic Cordillera. Tectonophysics 663, 310–321. https://doi.org/10.1016/j.tecto.2015.03.010.

Grand, S.P., 1987. Tomographic Inversion for Shear Velocity beneath the north American Plate. J. Geophys. Res. 92 (B13), 14065–14090. https://doi.org/10.1029/JB092iB13p14065.

Gurria, E., Mezcua, J., 2000. Seismic tomography of the crust and lithospheric mantle in the Betic Cordillera and Alboran Sea. Tectonophysics 329 (1–4), 99–119.

Hearn, T.M., 1996. Anisotropic Pn tomography in the western United States. J. Geophys. Res. 101 (B2), 8403–8414.

Holbrook, W.S., 1988. Wide-Angle Seismic Studies of Crustal Structure and Composition in Nevada, California and Southwest Germany. Ph.D. thesis. Stanford University.

Huang, Z., Zhao, D., Wang, L., 2015. P wave tomography and anisotropy beneath Southeast Asia: Insight into mantle dynamics. J. Geophys. Res. Solid Earth 120 (7), 5154–5174.

Humphreys, E., Clayton, R.W., 1988. Adaptation of back projection tomography to seismic travel time problems. J. Geophys. Res. Solid Earth 93 (B2), 1073–1085.

Informe, I.G.N., 2021. Informe de la actividad sísmica en Atarde-Santa Fe (Granada). Retrieved from. https://www.ign.es/resources/sismologia/noticias/InformeIGN_SantaFe.pdf.

Ishise, M., Kawakatsu, H., Shiomi, K., 2012. Revision of the 3-D anisotropic velocity structure of the Japan islands using Hi-net data: Northeastern Japan, B12–2. In: Programme and Abstracts of the 2012 Fall Meeting of Seismological Society of Japan, Hakodate, Japan.

Koulali, A., Ouzar, D., Tahayt, A., King, R.W., Vernant, P., Reilinger, R.E., McClusky, S., Mour-abit, T., Davila, J.M., Amraoui, N., 2011. New GPS constraints on active deformation along the Africa–Iberia plate boundary. Earth Planet. Sci. Lett. 308, 211–217. https://doi.org/10.1016/j.epsl.2011.05.048.

Liang, C., Liu, Z., Hua, Q., Wang, L., Jiang, N., Wu, J., 2020. The 3D seismic azimuthal anisotropies and velocities in the eastern Tibetan Plateau extracted by an azimuth-dependent dispersion curve inversion method. Tectonics 39, e2019TC005747. https://doi.org/10.1029/2019TC005747.

Liu, Y., Wu, S., Tong, P., 2022. Depth-dependent crustal azimuthal anisotropy in the Salton Trough, southern California. Tectonophysics 826, 229264.

Lozano, L., Cantavella, J.V., Gaite, B., Ruiz-Barajas, S., Antón, R., Barco, J., 2022. Seismic Analysis of the 2020–2021 Santa Fe seismic sequence in the Granada Basin, Spain: relocations and focal mechanisms. Seismol. Soc. Am. 93 (6), 3246–3265.

Madarieta-Txurruka, A., Galindo-Zaldívar, J., González-Castillo, L., Peláez, J.A., Ruiz-Armenteros, A.M., Henares, J., Gil, A.J., 2021. High-and low-angle normal fault activity in a collisional orogen: the Northeastern Granada Basin (Betic Cordillera). Tectonics 40 (7), e2021TC006715.

Madarieta-Txurruka, A., González-Castillo, L., Peláez, J.A., Catalán, M., Henares, J., Gil, A.J., Galindo-Zaldívar, J., 2022. The role of faults as barriers in confined seismic sequences: 2021 seismicity in the Granada Basin (Betic Cordillera). Tectonics 41 (9), e2022TC007481.

Martin-Rojas, I., Alfaro, P., Galindo-Zaldivar, J., Borque-Arancón, M.J., García-Tortosa, F.J., Sanz de Galdeano, C., Gil-Cruz, A.J., 2023. Insights of active extension within a collisional orogen from GNSS (Central Betic Cordillera, S Spain). Tectonics 42 (7), e2022TC007723.

Mori, J., Abercrombie, R.E., 1997. Depth dependence of earthquake frequency-magnitude distributions in California: implications for rupture initiation. J. Geophys. Res. Solid Earth 102 (B7), 15081–15090.

Paige, C.C., Saunders, M.A., 1982. LSQR: an algorithm for sparse linear equations and sparse least squares. ACM Transact. Math. Softw. (TOMS) 8 (1), 43–71.

Raitt, R.W., Shor Jr., G.G., Francis, T.J.G., Morris, G.B., 1969. Anisotropy of the Pacific upper mantle. J. Geophys. Res. 74 (12), 3095–3109.

Rodríguez-Fernández, J., de Galdeano, C.S., 2006. Late orogenic intramontane basin development: the Granada basin, Betics (southern Spain). Basin Res. 18 (1), 85–102.

Sanz de Galdeano, C., 2008. The Cadiz-Alicante Fault: an important discontinuity in the Betic Cordillera. Rev. Soc. Geol. Esp. 21 (3–4), 49–58.

Sanz de Galdeano, C., 2020. Main faults of the Betic Cordillera. Bol. Geol. Min. 131 (3), 373–385.

Sanz de Galdeano, C., Peláez, J.A., López Casado, C., 2003. Seismic potential of the main active faults in the Granada Basin (Southern Spain). Pure Appl. Geophys. 160 (8), 1537–1556. https://doi.org/10.1007/s00024-003-2359-3.

Sanz de Galdeano, C., García Tortosa, F.J., Peláez Montilla, J.A., Alfaro García, P., Azañón, J.M., Galindo Zaldívar, J., Ruano, P., 2012. Main Active Faults in the Granada and Guadix-Baza Basins (Betic Cordillera).
Schippkus, S., Zigone, D., Bokelmann, G., 2020. Azimuthal anisotropy in the wider Vienna basin region: a proxy for the present-day stress field and deformation. Geophys. J. Int. 220 (3), 2056–2067.
Serrano, I., Zhao, D., Morales, J., 2002. 3-D crustal structure of the extensional Granada Basin in the convergent boundary between the Eurasian and African plates. Tectonophysics 344 (1–2), 61–79.
Stich, D., Serpelloni, E., de Lis Mancilla, F., Morales, J., 2006. Kinematics of the Iberia–Maghreb plate contact from seismic moment tensors and GPS observations. Tectonophysics 426 (3–4), 295–317.
Stich, D., Martín, R., Morales, J., 2010a. Moment tensor inversion for Iberia–Maghreb earthquakes 2005–2008. Tectonophysics 483 (3–4), 390–398.
Stich, D., Martín, R., Morales, J., 2010b. Moment tensor inversion for Iberia–Maghreb earthquakes 2005–2008. Tectonophysics 483 (3–4), 390–398.
Thurber, C., Ritsema, J., 2015. Theory and observations - Seismic tomography and inverse methods. In: Schubert, Gerald (Ed.), Treatise on Geophysics, Second ed. Elsevier, pp. 307–337.
Utsu, T., 1984. Estimation of parameters for recurrence models of earthquakes. Bull. Earthq. Res. Inst., Univer. Tokyo 59, 53–66.
Vidal, F., 1986. Sismotectónica de la region Béticas-Mar de Alborán, Tesis Doctoral, 450 pp. Universidad de Granada, Granada.
Wang, J., Zhao, D., 2008. P-wave anisotropic tomography beneath Northeast Japan. Phys. Earth Planet. Inter. 170 (1–2), 115–133. ISSN 0031-9201,. https://doi.org/10.1016/j.pepi.2008.07.042.
Wang, J., Zhao, D., 2013. P-wave tomography for 3-D radial and azimuthal anisotropy of Tohoku and Kyushu subduction zones. Geophys. J. Int. 193 (3), 1166–1181. https://doi.org/10.1093/gji/ggt086.
Zhao, D., 2009. Multiscale seismic tomography and mantle dynamics. Gondwana Res. 15 (3–4), 297–323. ISSN 1342-937X. https://doi.org/10.1016/j.gr.2008.07.003.
Zhao, D., Hasewaga, A., Horiuchi, S., 1992. Tomographic imaging of P and S wave velocity structure beneath North-Eastern Japan. J. Geophys. Res. 97, 19,909–19,928.
Zhao, D., Mishra, O.P., Sanda, R., 2002. Influence of fluids and magma on earthquakes: seismological evidence. Phys. Earth Planet. Inter. 132, 249–267.
Zhao, D., Liu, X., Wang, Z., Gou, T., 2023. Seismic anisotropy tomography and mantle dynamics. Surv. Geophys. 44 (4), 947–982.